

INFRARED AND OPTICAL POLARIMETRY AROUND THE LOW-MASS STAR-FORMING REGION NGC 1333 IRAS 4A*

FELIPE O. ALVES^{1,6}, JOSÉ A. ACOSTA-PULIDO^{2,3}, JOSEP M. GIRART¹, GABRIEL A. P. FRANCO⁴, AND ROSARIO LÓPEZ⁵

¹ Institut de Ciències de l'Espai (IEEC-CSIC), Campus UAB, Facultat de Ciències, 08193 Bellaterra, Catalunya, Spain;

oliveira@ice.cat, girart@ice.cat

² Instituto de Astrofísica de Canarias, E-38200 La Laguna, Tenerife, Spain; jap@iac.es

³ Departamento de Astrofísica, Universidad de La Laguna, E-38205 La Laguna, Tenerife, Spain

⁴ Departamento de Física-ICEx-UFMG, 30.123-970 Belo Horizonte, Brazil; franco@fisica.ufmg.br

⁵ Departament d'Astronomia i Meteorologia (IEEC-UB), Institut de Ciències del Cosmos, Universitat de Barcelona, Martí i Franquès 1, E-08028 Barcelona, Spain; rosario@am.ub.es

Received 2011 February 1; accepted 2011 May 5; published 2011 June 14

ABSTRACT

We performed *J*- and *R*-band linear polarimetry with the 4.2 m William Herschel Telescope at the Observatorio del Roque de los Muchachos and with the 1.6 m telescope at the Observatório do Pico dos Dias, respectively, to derive the magnetic field geometry of the diffuse molecular cloud surrounding the embedded protostellar system NGC 1333 IRAS 4A. We obtained interstellar polarization data for about three dozen stars. The distribution of polarization position angles has low dispersion and suggests the existence of an ordered magnetic field component at physical scales larger than the protostar. Some of the observed stars present intrinsic polarization and evidence of being young stellar objects. The estimated mean orientation of the interstellar magnetic field as derived from these data is almost perpendicular to the main direction of the magnetic field associated with the dense molecular envelope around IRAS 4A. Since the distribution of the CO emission in NGC 1333 indicates that the diffuse molecular gas has a multi-layered structure, we suggest that the observed polarization position angles are caused by the superposed projection of different magnetic field components along the line of sight.

Key words: ISM: clouds – ISM: individual objects (NGC 1333) – ISM: magnetic fields – polarization – stars: individual (2MASS) – techniques: polarimetric

Online-only material: color figures

1. INTRODUCTION

Infrared and optical polarimetry is a suitable tool for observing magnetic fields within molecular clouds at large scales. At these wavelengths, polarization can be produced by dichroic extinction of background starlight. Davis & Greenstein (1951) proposed that a fraction of non-spherical interstellar dust grains become aligned perpendicular to the local magnetic field due to paramagnetic relaxation. Although this mechanism is commonly invoked in the literature, it seems to be inefficient within molecular clouds (e.g., Lazarian 2007). However, a more realistic scenario was proposed by several authors who have successfully modeled the perpendicular alignment between grains and magnetic fields by radiative torques propelled by anisotropic radiation (Draine & Weingartner 1996; Lazarian & Hoang 2007; Hoang & Lazarian 2008, 2009).

Aligned dust grains behave like a polarizer to any incoming radiation, absorbing and scattering the component of the electric field (*E*-vectors) parallel to their longest axis. Therefore, the observed radiation will carry some degree of linear polarization. The resulting polarization map outlines the geometry of the magnetic field lines projected onto the plane of sky (POS). Near-infrared (near-IR) polarimetric observations trace visual extinctions of a few tens of magnitudes, providing deeper photometry than optical wavelengths. However, the increase in interstellar extinction is not usually accompanied by a linear

increase in the degree of polarization. This has been interpreted as a decrease in the polarization efficiency, or depolarization, with increasing visual extinction (Goodman et al. 1992, 1995; Gerakines et al. 1995; Arce et al. 1998). Nevertheless, this depolarization at optical wavelengths is not observed in the Pipe Nebula (Franco et al. 2010) and submillimeter polarization observations show that there is unequivocal evidence that grains do align in dense environments with high visual extinction (e.g., Whittet et al. 2008; Vaillancourt et al. 2008). Additionally, the scattering of stellar light by dust grains also generates linear polarization in the optical and near-IR. This type of polarization is found in reflection nebulae associated with disks and envelopes of young stars.

NGC 1333 is the most active star-forming site in the Perseus molecular cloud (Lada et al. 1996). A large portion of the NGC 1333 young stellar cluster is composed by low-mass stars younger than 1 Myr (Wilking et al. 2004). In addition, there are numerous embedded protostars powering molecular and Herbig–Haro outflows (Knee & Sandell 2000). There is evidence that the molecular cloud in NGC 1333 is being disturbed by the large amount of outflow (Warin et al. 1996; Sandell & Knee 2001; Quillen et al. 2005).

The first polarimetric observations toward NGC 1333 were carried out by Vrba et al. (1976) and Turnshek et al. (1980). Tamura et al. (1988) conducted *K*-band polarimetric observations toward the center of the NGC 1333 reflection nebula. A larger polarimetric survey covering the full Perseus complex was carried out by Goodman et al. (1990). These observations show that there is a bimodal distribution of polarization position angle (P.A.), indicating that there are two large-scale magnetic field components along the line of sight.

* Based on observations collected with the 4.2 m William Herschel Telescope, at La Palma, Canary Islands (Spain) and the 1.6 m Telescope of the Observatório do Pico dos Dias, operated by Laboratório Nacional de Astrofísica (LNA/MCT, Brazil).

⁶ Present address: Argelander Institute for Astronomy, University of Bonn, Auf dem Hügel 71, 53121 Bonn, Germany; falves@astro.uni-bonn.de.

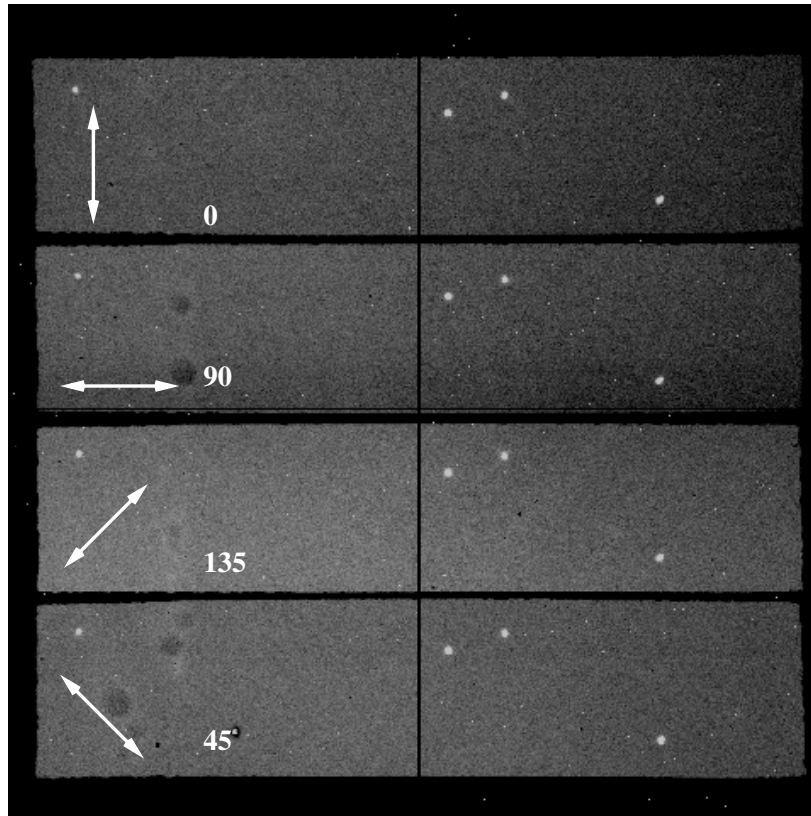


Figure 1. Typical CCD image in polarization mode. The four strips correspond to the 0° , 90° , 135° , and 45° polarization vectors from which the Stokes parameters are calculated.

NGC 1333 IRAS 4A (hereafter IRAS 4A), a low-mass protostellar system, has become the textbook case of a collapsing magnetized core: high angular resolution submillimeter polarimetric observations have revealed that the magnetic field has an hourglass morphology at scales of few hundred AUs (Girart et al. 1999, 2006). This is the magnetic field morphology predicted by theoretical models based on magnetically controlled molecular core collapse (e.g., Shu et al. 1987; Mouschovias 2001). Indeed, the synthetic polarization maps constructed using models of collapsing magnetized cores (Galli & Shu 1993; Shu et al. 2006) reproduced quite well the observations in IRAS 4A (Gonçalves et al. 2008). In this context, it is worth mentioning that it is still a question of ongoing debate whether magnetic fields or interstellar turbulence plays a major role in the dynamical evolution of a molecular cloud (e.g., Crutcher et al. 2009; Mouschovias & Tassis 2010).

In this paper, we report on one of the first scientific results obtained with the near-IR camera LIRIS (Acosta-Pulido et al. 2003; Machado et al. 2004) in its polarimetric mode. The observations were done using the *J*-band filter toward stars located relatively close to IRAS 4A ($\sim 4''$ – $8''$). The fields were selected to avoid the most active star-forming portion of the NGC 1333 cloud, so the measured polarized light is mainly due to dichroic absorption. In order to ascertain the quality of the near-IR data, we also provide complementary *R*-band linear polarimetry obtained with the Observatório do Pico dos Dias toward the same region. The scientific goal of this work is to compare the magnetic field observed in the IRAS 4A molecular core with the larger scale field associated with the cloud surrounding IRAS 4A. Girart et al. (2006) have already done this comparison but using very few distant stars ($\sim 14'$ – $20'$) retrieved from the Goodman et al. (1990) survey.

2. OBSERVATIONS

2.1. Near-infrared Observations

The near-IR observations were carried out in 2006 and 2007 December at the Observatorio del Roque de los Muchachos (La Palma, Canary Islands, Spain). The LIRIS camera, attached to the Cassegrain focus of the 4.2 m William Herschel Telescope (WHT), is equipped by a Hawaii detector of 1024×1024 pixels optimized for the 0.8 – $2.5 \mu\text{m}$ range.

LIRIS is capable of performing polarization observations by using a wedged double Wollaston device, WeDoWo, which is composed by a combination of two Wollaston prisms and two wedges (see Oliva 1997, for detailed description). In this observing mode, the polarized flux is measured simultaneously at four different angles (0° , 45° , 90° , and 135°). An aperture mask of $4' \times 1'$ is used in order to avoid overlapping between the different polarization images. Figure 1 shows a typical LIRIS image in polarimetric mode. The degree of linear polarization can thus be determined from data taken at the same time and with the same observing conditions. In order to achieve accurate sky subtraction, a five-point dither pattern was used. Offsets of about $20''$ were adopted along the horizontal, long mask direction. During the 2006 and 2007 campaigns, we took seven and six exposures, respectively, of 20 s per dither position. The five-point dither cycle was repeated several times until completion of the observation. The total observing time for each field was 2800 s in 2006 and 2400 s in 2007.

We carried out *J*-band polarization observations of ten fields, six of them with the telescope rotator at 0° and four with the rotator at 90° (see Table 1). Figure 2 indicates the observed fields as black and red rectangles, corresponding to observations with rotator at 0° and 90° , respectively. We covered the area surveyed

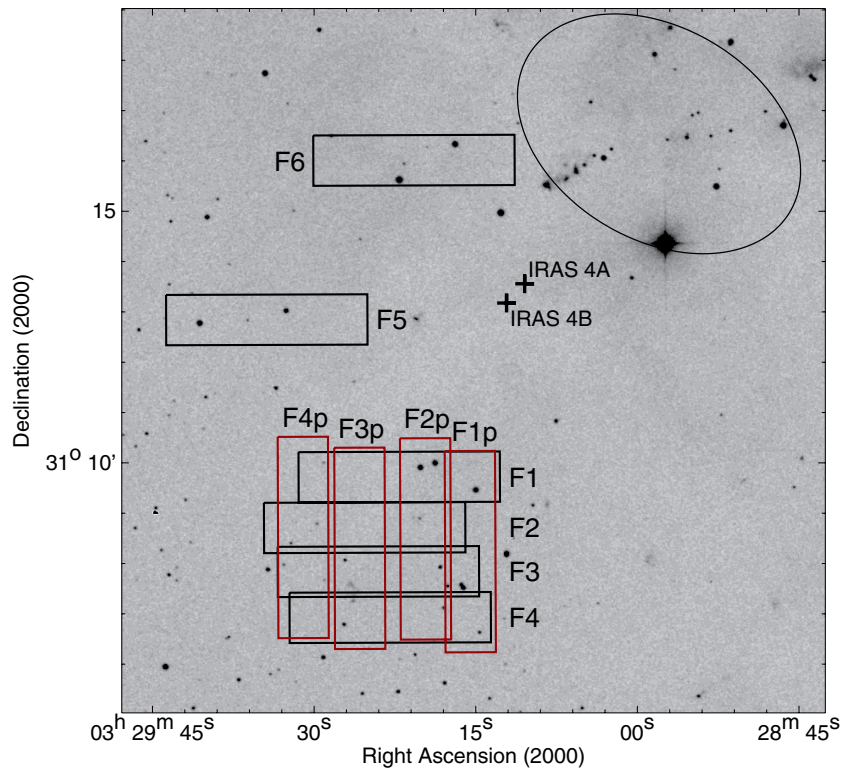


Figure 2. DSS *R*-band image of our science targets. Black boxes are observed fields with rotator at 0° while red boxes are observed fields at 90° . Crosses mark the positions of the protostars NGC 1333 IRAS 4A and NGC 1333 IRAS 4B. The ellipse in the upper right corner indicates the star-forming region, where no science targets were selected in order to avoid polarization data due to dust scattering.

(A color version of this figure is available in the online journal.)

Table 1
Log of the Observations^a

Target ID	α_{2000} (hh:mm:ss.ss)	δ_{2000} (dd:mm:ss.ss)	Obs. Date	Rotator ($^\circ$)
F1	03:29:22.01	+31:09:42.12	2006 Dec 26	0
F2	03:29:25.24	+31:08:41.88	2006 Dec 26	0
F3	03:29:23.98	+31:07:49.41	2006 Dec 26	0
F4	03:29:22.90	+31:06:54.62	2006 Dec 26	0
F5	03:29:34.26	+31:12:50.08	2007 Dec 13	0
F6	03:29:20.52	+31:15:59.63	2007 Dec 13	0
F1p	03:29:15.44	+31:08:12.82	2006 Dec 26	90
F2p	03:29:19.59	+31:08:28.20	2007 Dec 13	90
F3p	03:29:25.70	+31:08:17.24	2007 Dec 13	90
F4p	03:29:30.95	+31:08:30.44	2007 Dec 13	90

Note. ^a The night of 2006 December 27 had very limited weather conditions and only calibrators were observed.

by observing with the rotator at 0° and 90° , except for the two upper fields. This procedure allows us to compare both data sets and, consequently, to achieve higher precision in the estimated polarization parameters.

2.2. Optical Observations

The optical *R*-band linear polarimetry was performed using the 1.6 m telescope of the Observatório do Pico dos Dias (LNA/MCT, Brazil) during observing runs conducted in 2007 and 2008. A specially adapted CCD camera composed by a half-wave rotating retarder followed by a calcite Savart plate and a filter wheel was attached to the focal plane of the telescope. The half-wave retarder can be rotated in steps of 22.5°

and one polarization modulation cycle is fully covered after a complete 90° rotation. The birefringence property of the Savart plate divides the incoming light beam into two perpendicularly polarized components: the ordinary and extraordinary beams. From the difference in the measured flux for each beam one estimates the degree of polarization and its orientation in the plane of the sky. For a technical description of this polarimetric unit, we refer the interested reader to the work by Magalhães et al. (1996). The obtained optical data are part of an ongoing large-scale ($\sim 1 \text{ deg}^2$) survey whose results will be discussed in a forthcoming paper (G. A. P. Franco et al. 2011, in preparation). The area covered by the optical survey overlaps the portion of the sky observed in near-IR, and in order to make a comparative analysis of the results obtained at both wavelengths, we included the optical results gathered for stars lying in the overlapped area in the discussion.

3. LIRIS DATA REDUCTION AND CALIBRATION

The near-IR data reduction was performed using the *lirisdr* package developed by the LIRIS team in the IRAF environment.⁶ Given the particular geometry of the frames (see Figure 1), the first procedure was to slice the image into four frames. Each set of frames corresponding to a given polarization state is processed independently. The data reduction process comprises sky subtraction, flat-fielding, geometrical distortion correction, and finally co-addition of images after registering. A second background subtraction was performed upon flat-fielded images in order to avoid the residuals introduced by

⁶ IRAF is distributed by the National Optical Astronomy Observatory, which is operated by the Association of Universities for Research in Astronomy, Inc., under cooperative agreement with the National Science Foundation.

the vertical gradient due to the reset anomaly effect associated with the Hawaii arrays (e.g., Acosta-Pulido et al. 2006). An approximate astrometric solution was determined based on the image header parameters.

3.1. Photometry

Aperture photometry of the field stars in each slice was obtained using the task Object Detection, available within Starlink GAIA software.⁷ The aperture radius used was $\sim 4''$, which corresponds to three times the median seeing of the night. The background was extracted from an annulus with an inner radius of $6''$ and an outer radius of $8''$. The astrometric solution of each slice was tweaked using the astrometric tools available within the Starlink GAIA software. We used the 2MASS catalog to perform the photometric and astrometric calibrations. In our sample, we reached J magnitudes as faint as ~ 17 . As a final step, we identified the counterparts of each object in the four slices in order to compute the polarization properties. In some cases, matching of stars observed with rotator at 0° and 90° was also necessary since some objects were present in both sets of observations.

3.2. Polarimetric Analysis

Using the WeDoWo, we simultaneously measured four polarization states in each of the strips as

$$i_0[\text{P.A.} = 0] = \frac{1}{2} t_0 (I_* + Q_*) \quad (1)$$

$$i_{90}[\text{P.A.} = 0] = \frac{1}{2} t_{90} (I_* - Q_*) \quad (2)$$

$$i_{45}[\text{P.A.} = 0] = \frac{1}{2} t_{45} (I_* + U_*) \quad (3)$$

$$i_{135}[\text{P.A.} = 0] = \frac{1}{2} t_{135} (I_* - U_*), \quad (4)$$

where I_* , Q_* , and U_* are the Stokes parameters of the object to be measured, and the factors $t_{0,90,45,135}$ represent the transmission for each polarization state. In this case, the normalized Stokes parameters can be determined by

$$q_* = \frac{i_0 - i_{90} t_{0/90}}{i_0 + i_{90} t_{0/90}} \quad (5)$$

$$u_* = \frac{i_{45} - i_{135} t_{45/135}}{i_{45} + i_{135} t_{45/135}}, \quad (6)$$

where the factors $t_{0/90}$ and $t_{45/135}$ measure the relative transmission of the ordinary and extraordinary rays for each Wollaston. These factors were calibrated using non-polarized standards and resulted in the values $t_{0/90} = 0.997$ and $t_{45/135} = 1.030$, with an uncertainty of about 0.002 in both cases.

The rotation of the whole instrument by 90° causes the exchange of the optical paths for the orthogonal polarization vectors. Now, the resulting polarization states are given by

$$i_0[\text{P.A.} = 90] = \frac{1}{2} t_0 (I_* - Q_*) \quad (7)$$

$$i_{90}[\text{P.A.} = 90] = \frac{1}{2} t_{90} (I_* + Q_*) \quad (8)$$

$$i_{45}[\text{P.A.} = 90] = \frac{1}{2} t_{45} (I_* - U_*) \quad (9)$$

$$i_{135}[\text{P.A.} = 90] = \frac{1}{2} t_{135} (I_* + U_*). \quad (10)$$

This effect can be used in order to get a more accurate estimate of the Stokes parameters because the combination of both measurements, P.A. = 0° and 90° , results in the cancellation of the transmission factors and reduces flat-field uncertainties. The normalized Stokes parameters are then computed by

$$q_* = \frac{R_Q - 1}{R_Q + 1}, \text{ being } R_Q^2 = \frac{i_0[\text{P.A.} = 0]/i_{90}[\text{P.A.} = 0]}{i_0[\text{P.A.} = 90]/i_{90}[\text{P.A.} = 90]} \quad (11)$$

$$u_* = \frac{R_U - 1}{R_U + 1}, \text{ being } R_U^2 = \frac{i_{45}[\text{P.A.} = 0]/i_{135}[\text{P.A.} = 0]}{i_{45}[\text{P.A.} = 90]/i_{135}[\text{P.A.} = 90]}. \quad (12)$$

Finally, after estimation of the q and u Stokes parameters, the degree of linear polarization and the position of polarization angle (measured eastward with respect to the north celestial pole) are calculated as

$$p = \sqrt{q_*^2 + u_*^2} \quad (13)$$

$$\theta = \frac{1}{2} \tan^{-1} \left(\frac{u_*}{q_*} \right).$$

Flux errors in i_0 , i_{90} , i_{45} , and i_{135} are dominated by photon shot noise, while the theoretical error in polarization fraction was estimated performing error propagation through the previous equations. In addition, we calculated the errors in p using a Monte Carlo method, which returned values similar to those estimated from error propagation. The 1σ uncertainty in θ was estimated (1) by applying the relation derived by Serkowski (1974) using standard error propagation, that is, $\sigma_\theta = 28.65\sigma_p/p$, when $p/\sigma_p \geq 5$ or (2) graphically with the aid of the curve proposed by Naghizadeh-Khouei & Clarke (1993) when $p/\sigma_p < 5$.

Figure 3 shows the polarization uncertainty as a function of the J -band magnitude achieved with our LIRIS observations. The observed distribution suggests that the uncertainties are dominated by photon shot noise, as expected for a sample collected with fixed exposure time. As expected, the uncertainties decrease when the data taken at 0° and 90° are combined. There is a natural limit which is due to the uncertainty bias when measuring low levels of polarization. Bias in the degree of linear polarization (p) comes from the fact that this quantity is defined as a quadratic sum of q and u , which produces a non-zero polarization estimate due to the uncertainties in their measurement (for a detailed discussion see for instance, Simmons & Stewart 1985; Wardle & Kronberg 1974). In order to remove the polarization bias and compute the true polarization, we used the prescription proposed by Simmons & Stewart (1985) for low polarization stars. The true polarization degree can be approximated by the expressions $p_{\text{true}} = 0$ if $p_{\text{obs}}/\sigma_p < K_a$, otherwise $p_{\text{true}} = (p_{\text{obs}}^2 - \sigma_p^2 \cdot K_a^2)^{1/2}$. We adopted $K_a = 1$, which corresponds to the estimator defined by Wardle & Kronberg (1974).

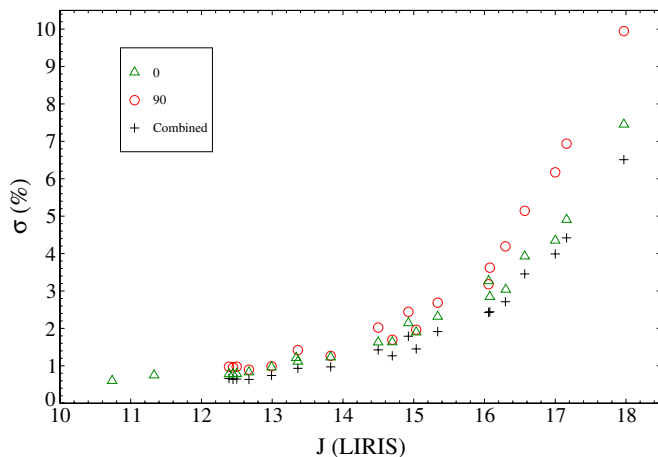
3.3. Standard Stars

Observations of polarized and unpolarized standard stars were taken in order to calibrate the instrumental characteristics of

⁷ GAIA is a derivative of the Skycat catalog and image display tool, developed as a part of the Very Large Telescope project at ESO.

Table 2
Standard Stars

ID	α_{2000} (hh:mm:ss.sss)	δ_{2000} (dd:mm:ss.ss)	Type	P (%)	θ^a ($^\circ$)	Filter	Ref.
CMa R1 No. 24 ^b	07:04:47.364	-10:56:17.44	Polarized	2.1 ± 0.05	86 ± 1	J	1
BD+28d4211	21:51:11.070	+28:51:51.80	Unpolarized	0.041 ± 0.031	38.66	N ^c	2
				0.067 ± 0.023	135.00	U	2
				0.063 ± 0.023	30.30	B	2
				0.054 ± 0.027	54.22	V	2
G191B2B	05:05:30.621	+52:49:51.97	Unpolarized	0.065 ± 0.038	91.75	U	2
				0.090 ± 0.048	156.82	B	2
				0.061 ± 0.038	147.65	V	2

Notes.^a Position angles measured from north to east.^b This is the only polarized standard star with well established polarization properties in the J band.^c “Near-UV” filter centered in 3450 Å and with full width at half-maximum (FWHM) bandpass of 650 Å. For details, see Schmidt et al. (1992).**References.** (1) Whittet et al. 1992; (2) Schmidt et al. 1992, the two unpolarized stars are taken from a compilation of optical calibration data collected with the *Hubble Space Telescope*.**Figure 3.** Distribution of the polarization uncertainty (σ_P) with respect to the J magnitude obtained for each field star with the telescope rotator at 0° (green triangles), 90° (red circles), and a combination of both (crosses). This plot contains only stars whose signal-to-noise ratio of the combined setup (crosses) is better than 1 (except for three stars that also have a signal-to-noise ratio better than 1 but which were only observed with the rotator at 0° , see Table 5). Note that uncertainties are lower when the combination of images taken with the telescope rotator at 0° and 90° is used. The large discrepancy observed between 0° and 90° errors for some stars are due to the distinct observation epochs of each data set.

(A color version of this figure is available in the online journal.)

LIRIS in its polarimetric mode. Table 2 summarizes the general information for these stars: Columns 1–8 indicate their name, equatorial coordinates, type, polarization degree, and position angle, the filter used for the polarization measurements and the reference, respectively. Unpolarized standard stars were observed to check for any possible instrumental polarization and for systematic errors in our polarimetry. The unpolarized stars G191B2B and BD+28d4211 were observed with rotator at 0° and 90° . The polarized intensity measured for the two unpolarized standards was very small (see Table 3). The measured normalized Stokes q and u were 0.051% and 0.226%, respectively, with the rotator at 0° , and -0.117% and 0.119% , respectively, with the rotator at 90° . Table 3 shows the observed polarization degree before and after bias correction for the two unpolarized standards. The measurements taken in the two epochs for BD+28d4211 give consistent values. We applied the method proposed by Simmons & Stewart (1985) for a 99%

Table 3
Observational Results for the Unpolarized Standard Stars

ID	Mission	P_{obs} (%)	P/σ	P_{true}	$P_{\text{min}}/P_{\text{max}}^a$ (%)
G191B2B	2007	0.41	1.38	0.28	0.00/1.10
BD+28d4211	2006	0.09	0.60	0.00	0.00/0.41
BD+28d4211	2007	0.15	1.17	0.08	0.00/0.45

Note. ^a Minimum and maximum values for the degree of polarization at 99% confidence level (Simmons & Stewart 1985).**Table 4**
Observational Results for the Polarized Standard Star

ID	P_{obs} (%)	σ_P (%)	P/σ	P_{true} (%)	$P_{\text{min}}/P_{\text{max}}^a$ (%)	θ_{obs} ($^\circ$)	σ_θ ($^\circ$)
CMa R1	2.10	0.26	7.98	2.08	1.38/ 2.78	92.7	4
No 24	2.04	0.26	7.99	2.02	1.35/2.70	94.3	4
	2.33	0.26	9.06	2.31	1.62/3.00	93.5	3
	2.05	0.22	9.43	2.04	1.44/ 2.62	86.8	3

Note. ^a Minimum and maximum values for the degree of polarization at 99% confidence level (Simmons & Stewart 1985).

confidence level for the observed unpolarized standards. This resulted in a small, if any, instrumental polarization.

The polarized standard star CMa R1 No. 24 was observed in order to verify the zero point of the polarization position angles. Table 4 summarizes the results obtained for the four measurements conducted for this object. As expected, high-quality data are less sensitive to biasing, and the unbiased polarization has basically the same values of the observed polarization. Taking into account the uncertainties, we see that our J -band data match the result obtained by Whittet et al. (1992). The difference between the average P.A. obtained for these four measurements and that obtained by Whittet et al. (1992) is $\sim 6^\circ$, which is very close to the statistical deviation of our measurements thus discarding any further correction for the zero angle calibration.

4. POLARIZATION PROPERTIES

4.1. Infrared Data

Table 5 contains a summary of our near-IR and optical polarization data for stars with a signal-to-noise ratio in the

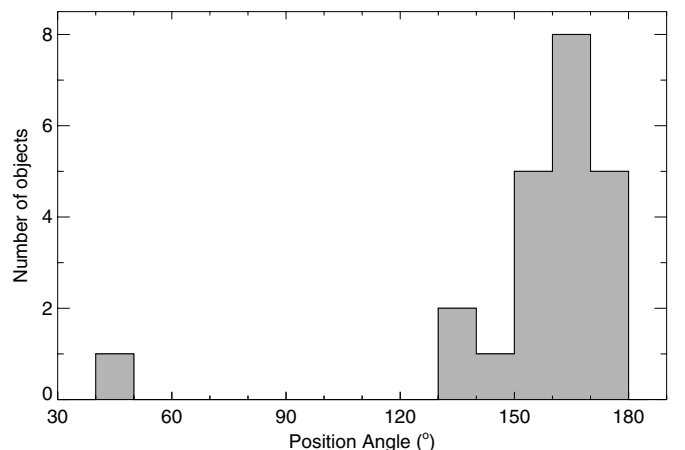
Table 5
Polarization Data

ID	α_{2000} (hh:mm:ss.ss)	δ_{2000} (dd:mm:ss.ss)	J^a (mag)	p^R (%)	σ_{p^R} (%)	θ^{Rb} ($^\circ$)	p^J (%)	σ_{p^J} (%)	p_{true}^J (%)	θ^{Jb} ($^\circ$)	σ_{θ^c} ($^\circ$)	Rotator Position ($^\circ$)	Class ^d
1	03:29:14.58	31:06:38.20	14.70	4.04	0.75	151.5	1.74	1.27	1.41	173	27	0.90	IR source
2	03:29:14.89	31:09:27.50	12.67	4.53	0.06	157.8	3.10	0.64	3.03	157	7	0.90	Star
3	03:29:15.05	31:08:06.90	16.06				3.16	2.43	2.02	160	33	0.90	IR source
4	03:29:16.08	31:07:31.40	12.99	4.51	0.12	166.2	2.32	0.74	2.20	172	10	0.90	IR source
5	03:29:16.20	31:07:34.00	13.83	3.92	0.21	157.6	1.88	0.97	1.61	167	18	0.90	...
6	03:29:16.68	31:16:18.30	10.74	0.87	0.14	117.5	1.67	0.60	1.56	135	11	0	IR source
7	03:29:17.52	31:07:33.20	15.04	3.88	0.25	163.3	1.82	1.45	1.10	171	37	0.90	IR source
8	03:29:17.91	31:07:07.70	15.34				2.70	1.91	1.90	169	29	0.90	IR source
9	03:29:18.21	31:07:55.70	14.50	3.32	0.48	167.2	2.55	1.43	2.11	163	20	0.90	IR source
10	03:29:18.64	31:09:59.60	12.50	4.40	0.04	156.4	4.68	0.65	4.63	155	4	0.90	Star
11	03:29:20.01	31:09:54.30	12.45	5.75	0.10	164.0	4.89	0.64	4.85	160	4	0.90	Star
12	03:29:20.10	31:08:54.00	16.08				3.15	2.44	1.99	155	33	0.90	...
13	03:29:21.87	31:15:36.30	11.33	0.94	0.09	49.4	1.60	0.75	1.41	49	16	0	CTTS ^e
14	03:29:23.50	31:07:25.00	16.57				4.54	3.46	2.94	167	33	0.90	...
15	03:29:24.70	31:07:27.00	17.16				4.56	4.42	1.12	167	24	0.90	...
16	03:29:25.60	31:08:43.00	17.00				4.90	3.99	2.85	172	23	0.90	IR source
17	03:29:27.04	31:08:04.60	12.39	4.61	0.29	157.6	3.53	0.66	3.47	169	6	0.90	IR source
18	03:29:27.16	31:06:48.20	14.92	5.20	0.51	166.1	3.32	1.79	2.80	173	20	0.90	IR source
19	03:29:28.99	31:10:00.30	13.36				4.01	0.93	3.90	142	7	0.90	IR source
20	03:29:29.60	31:08:47.90	16.30				3.17	2.71	1.64	156	42	0.90	IR source
21	03:29:30.80	31:06:33.00	17.97				7.01	6.51	2.61	160	25	0.90	IR source
22	03:29:32.41	31:13:01.10	13.34				1.90	1.21	1.47	135	24	0	IR source
Stars with <i>R</i> -band data only													
23	03:29:02.87	31:16:00.82	12.84	0.68	0.15	66.4							YSOC
24	03:29:03.74	31:16:03.60	11.74	7.58	0.54	57.7							V512 Per
25	03:29:04.04	31:17:06.66	13.31	1.38	0.52	86.3							BD ^f
26	03:29:07.39	31:10:49.02	13.10	3.11	0.17	167.0							Star
27	03:29:09.57	31:09:08.68	14.94	4.61	0.61	161.1							Star
28	03:29:12.16	31:08:10.91	12.99	0.39	0.08	71.8							IR source
29	03:29:17.84	31:05:37.40	14.04	4.35	0.45	164.4							IR source
30	03:29:20.59	31:06:11.48	15.28	5.13	0.93	174.5							IR source
31	03:29:29.11	31:06:08.77	14.07	5.36	0.32	167.3							IR source
32	03:29:34.24	31:07:53.33	13.64	2.15	0.39	153.7							IR source
33	03:29:39.77	31:14:51.61		1.38	0.19	13.6							...
34	03:29:40.43	31:12:46.38	13.04	0.34	0.06	41.4							IR source

Notes.^a LIRIS *J* magnitude for stars observed with this camera, 2MASS *J* magnitude for stars observed only in the *R* band.^b Position angles are counted from north to east.^c 1σ uncertainty of the position angle (see the text for explanation on how it was estimated).^d Object's type as found in the SIMBAD Astronomical Database.^e Classical T-Tauri Star (Lada et al. 1974).^f Brown Dwarf (Itoh et al. 2010).

polarization intensity higher than unity. Column 1 gives the star's identification number in our catalog. Columns 2 and 3 show the equatorial coordinates. Column 4 gives the *J*-band magnitude. Columns 5–12 show the polarization degree and the polarization P.A. (with their uncertainties) for the *R* and *J* bands. The last two columns indicate the rotator position used to acquire the near-IR data, and the object type, respectively. Figure 4 shows that, excluding star 13, the polarization P.A. distribution measured in the *J* band is quite narrow with a mean position angle of 160° and a standard deviation of only 12° . We note that the *J*-band polarization uncertainties may be overestimated. First, the aforementioned standard deviation is about half the mean 1σ uncertainty of the polarization P.A., and second, there is a very good agreement between the near-IR and optical data (see the next section).

Figure 5 shows the spatial distribution of the near-IR polarization vectors overlaid on the 2MASS *J*-band image. The

**Figure 4.** Distribution of polarization angles of the near-IR data. The histogram is binned in 10° .

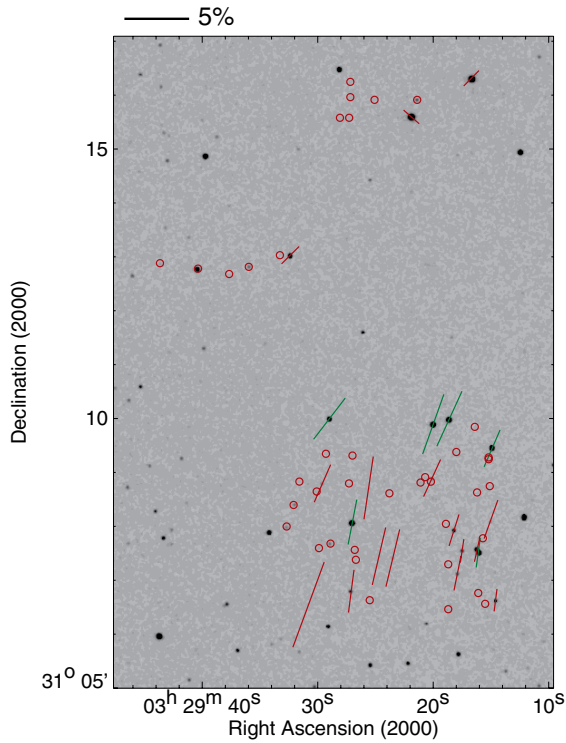


Figure 5. *J*-band polarization vectors in NGC 1333 plotted over a 2MASS *J*-band image. Vector length scale is shown on the upper left corner. Green vectors indicate stars with $P/\sigma_P > 3$ while red vectors have $1 < P/\sigma_P < 3$. Open circles indicate positions of observed objects with $P/\sigma_P < 1$. Some of the detected polarized stars in the *J* band do not have a 2MASS counterpart, indicating that the obtained LIRIS data probe deeper visual extinctions in the cloud than the 2MASS.

polarized stars with a declination below $31^\circ 10'$ have larger polarization degrees than those above this value. This subsample comprises most of stars with mean P.A. $\simeq 160^\circ$. Star number 13 is the only object in our catalog presenting intrinsic polarization (see Section 5).

4.2. Comparison with Optical Data

Previous optical polarimetric observations performed toward the field of view shown in Figure 5 detected only two polarized stars of the *J*-band sample, stars number 2 and 13 (Vrba et al. 1976; Menard & Bastien 1992), and our data are in good agreement with them. The *R*-band polarimetric sample has 12 stars in common with our near-IR data. Figure 6 shows the polarization vectors in both bands plotted over a Digitized Sky Survey (DSS) image. There is noticeably good agreement between the two polarization data sets (see also Figure 7). Thus, the mean value of the P.A. difference between the *R* and *J* band for the 12 stars is 6.5° .

Figure 8 represents the resulting P_{NIR} versus P_{visible} diagram for the 12 stars with both *J* and *R* polarimetric measurements. The wavelength at which the polarization is highest, λ_{max} , is related to the mean size of the interstellar grains responsible for producing the observed polarized light (Serkowski et al. 1975; McMillan 1978). The typical value of λ_{max} observed for the diffuse interstellar medium is $0.55 \mu\text{m}$ (Serkowski et al. 1975). However, in molecular clouds λ_{max} appears to change with the visual extinction (Andersson & Potter 2007). In the case of NGC 1333, it has been shown that λ_{max} changes between 0.66 and $0.89 \mu\text{m}$ (Turnshek et al. 1980; Černis 1990; Whittet et al. 1992). The two solid lines in Figure 8 show the expected relation for $\lambda_{\text{max}} = 0.55$ and $0.86 \mu\text{m}$. The data do not show

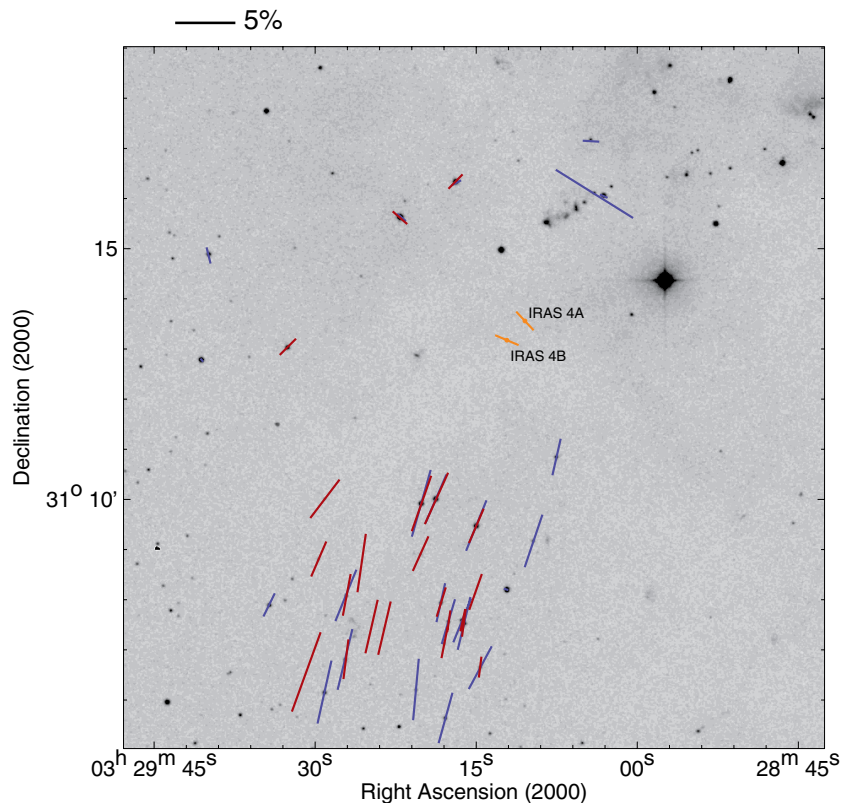


Figure 6. Comparison between optical (blue vectors) and near-IR (red vectors) data. The polarimetric map is plotted over a DSS *R*-band image. The vector length scale is shown on the upper left corner. Orange vectors represent the averaged magnetic field of IRAS 4A and IRAS 4B, as obtained by submillimeter observations of Attard et al. (2009).

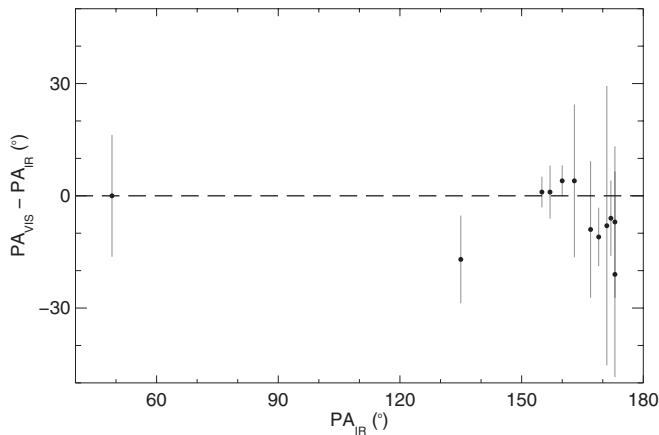


Figure 7. Comparative diagram of the position angles obtained for the optical (R -band) and near-IR (J -band) data sets.

any preferential regime of maximum polarization due to the low statistics. Polarization observations over a wider range of wavelengths are necessary to refine this characterization.

5. POLARIZATION FROM YSOs AND FOREGROUND STARS

Our near-IR and optical maps are characterized by a uniform component predominant to the south of the IRAS 4A/4B double system (see Figure 6). However, north of IRAS 4A/4B the few detected polarized stars have a broader angle distribution. Most of these stars are likely young stellar objects (YSOs). In these cases, the polarization is produced by intrinsic scattering within circumstellar disks rather than by interstellar absorption. Several authors have studied the physical properties of YSOs by means of polarimetry (e.g., Brown & McLean 1977; Mundt & Fried 1983) and, in general, observations suggest that near-IR polarization vectors, when produced by single scattering, are oriented perpendicularly to optically thin disks, while multiple scattering within optically thick disks generates polarization vectors whose P.A. are parallel to their long axis (Angel 1969; Bastien & Menard 1990; Pereyra et al. 2009).

The YSOs possibly showing intrinsic polarization in the near-IR and/or R band are listed below.

1. LkH α 271 (star no. 13 of Table 5) is a Classical T Tauri star (Lada et al. 1974). The near-IR polarization angle and degree are in excellent agreement with the R -band data. Previous observations showed that the polarization varies considerably, which has been interpreted as arising from outbursts or inhomogeneities in a circumstellar shell within an optically thick circumstellar disk (Tamura et al. 1988; Menard & Bastien 1992).
2. SVS 13A (star no. 24) was observed only in the R band. The obtained polarization is in excellent agreement with the value previously measured in the K band ($P_K = 7.2\% \pm 0.9\%$ and $P.A. = 56^\circ \pm 4^\circ$; Tamura et al. 1988). This object is a well-studied source (Rodríguez et al. 2002; Anglada et al. 2004; Chen et al. 2009) which powers a bipolar and collimated outflow associated with the well-known Herbig–Haro objects HH 7-11 (Herbig 1974; Strom et al. 1974). The orientation of the outflow is roughly perpendicular to the polarization P.A., which suggests that the disk is optically thick.
3. 2MASS J03290289+3116010 (star no. 23) is close to SVS 13A and has a very low degree of polarization.

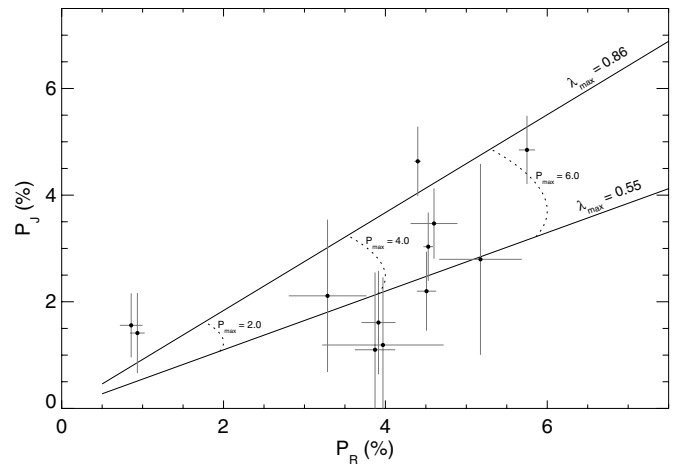


Figure 8. Spectral energy distribution of the observed linear polarization in near-IR and visible. Solid lines indicate constant λ_{\max} of 0.55 and 0.86 μm from bottom to top, respectively. Dashed lines represent constant p_{\max} of 2%, 4%, and 6% from the origin going outward, respectively.

According to the SIMBAD Astronomical Database, this is a bright ($J \simeq 12.8$) K-type star and it is possibly a foreground star. In fact, previous spectral analysis and photometric studies place this star at a distance of only ~ 50 pc from the Sun (Aspin et al. 1994; Aspin 2003).

4. ASR 8 (star no. 25) is classified as a brown dwarf by SIMBAD. However, an extensive survey on the evolutionary state of stars in NGC 1333 identifies this object as a T Tauri star with a mass of $0.7 M_\odot$ (Aspin 2003), which is reinforced by the presence of X-ray emission (Getman et al. 2002). We therefore attribute the optical polarization measured for this star due to intrinsic scattering.

In addition, there are two bright infrared stars ($J \lesssim 13.0$) with low polarization (stars no. 28 and 34 in Table 5) that are apparently not associated with YSOs, as no star formation or nebulosity signs has been reported in the literature. Their 2MASS color indices suggest that they may be unreddened M-type dwarf stars, which is also corroborated by the low degree of polarization. We therefore consider these objects to be foreground stars.

6. THE MAGNETIC FIELD IN NGC 1333

6.1. The Distribution of Dust and Molecular Gas in NGC 1333

The most detailed picture of the distribution of gas and dust in the Perseus cloud has been provided by the COMPLETE project (Ridge et al. 2006b; Pineda et al. 2008), a survey of near/far-IR extinction data, and of atomic, molecular, and thermal dust continuum emission obtained over a large area. These data show a wide range of visual magnitudes for NGC 1333, and a non-Gaussian CO spectral profile consistent with multi-velocity components. These results are consistent and likely related to a layered cloud structure along the line of sight, which was first proposed by Ungerechts & Thaddeus (1987). Interstellar extinction studies of field stars toward NGC 1333 also suggest at least two components in the line of sight at different distances toward NGC 1333 (Černis 1990).

According to column density maps of the Perseus cloud (Ridge et al. 2006a), the region studied here lies in the lower density envelope of NGC 1333. Maps of high density molecular tracers (N_2H^+ , HCO^+) as well as of the 870 μm dust emission

show that around IRAS 4A the dense gas has a filamentary distribution oriented in the NW–SE direction, with the long axis positioned at $\simeq 142^\circ$ (Sandell & Knee 2001; Olmi et al. 2005; Walsh et al. 2007).

6.2. The Field Morphology as Traced by the Diffuse Gas

The near-IR and optical polarization vectors of the background stars shown in Figure 6 trace the POS component of the magnetic field associated with the lower density envelope around IRAS 4A/4B. South of these sources, where we have most of the polarization sample, the magnetic field has a direction of $\simeq 160^\circ$. The observed configuration is consistent with the results obtained at much larger scale by Goodman et al. (1990) and Tamura et al. (1988). According to the COMPLETE survey (Ridge et al. 2006b) the polarization was measured toward regions with a visual extinction of 4–5 mag.

The magnetic field orientation derived from our data is roughly parallel to the dense filamentary structure associated with IRAS 4A (Sandell & Knee 2001; Walsh et al. 2007). However, the submillimeter polarization maps toward IRAS 4A and IRAS 4B show that the magnetic field within the filament is approximately perpendicular to the filament’s major axis (Girart et al. 1999, 2006; Attard et al. 2009), and is therefore perpendicular to the magnetic field direction traced by our optical and near-IR data. The single-dish submillimeter polarization map from Attard et al. (2009) around IRAS 4A is associated with visual extinctions as low as ~ 10 mag, which is a typical value for near-IR extinction data. Therefore, the submillimeter and near-IR/optical data seem to reveal substantial changes in the magnetic field topology between the dense filament and the diffuse molecular envelope that surrounds it. Such a sharp twist in the field is hard to explain by means of structural changes in the magnetic field only, because within the observed field, the position angle of the optical and near-IR polarimetric data is quite uniform (see Figure 4). Instead, the two data sets may be simply tracing distinct gas components. As explained in Section 6.1, there is observational evidence of a multi-component structure for the NGC 1333 molecular cloud. Figure 9 shows the ^{12}CO and ^{13}CO spectra extracted from a box containing the region studied here. These spectra show at least three distinguishable velocity components: a faint emission centered at $v_{\text{LSR}} \simeq 2 \text{ km s}^{-1}$ (seen more clearly in the ^{12}CO data), the peak of the ^{13}CO data centered at $\sim 7.6 \text{ km s}^{-1}$, and the peak of the ^{12}CO data at $\sim 6.7 \text{ km s}^{-1}$. This last component has the same v_{LSR} of the IRAS 4A dense core (Choi 2001). Therefore, whereas the submillimeter polarization measurements trace only the molecular cloud component associated with the IRAS 4A dense core, the near-IR and optical polarimetric data are probably tracing the mean magnetic field of the different velocity molecular cloud components observed in the CO maps. Nevertheless, further observations are needed in order to obtain a more complete description of the magnetic field in this region.

7. CONCLUSIONS

We have carried out one of the first polarimetric observations in the *J*-band collected with the WHT/LIRIS infrared camera. We also present *R*-band linear polarimetry obtained at the Observatório do Pico dos Dias. We observed an area of $\sim 6' \times 4'$ around the NGC 1333 IRAS 4A/4B protostellar system. The main conclusions of this work are as follows.

1. The infrared polarization map derived for the surveyed area is highly consistent with the optical map obtained with a

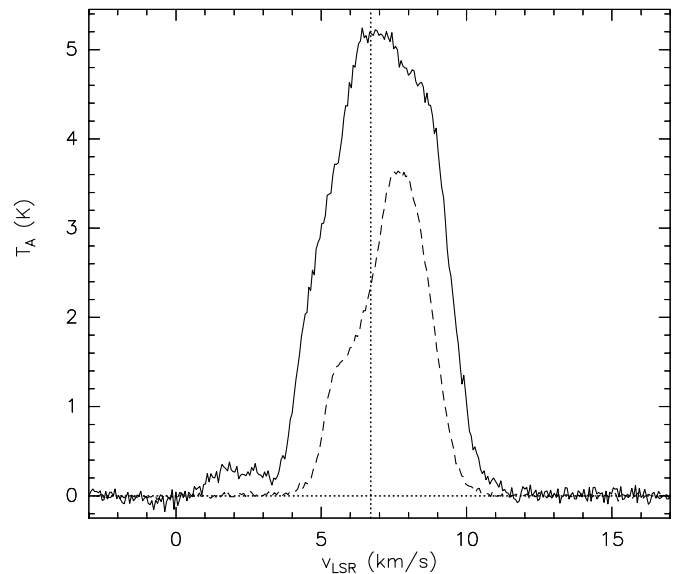


Figure 9. Averaged spectra of the ^{12}CO 1–0 (solid line) and the ^{13}CO 1–0 (dashed line) lines obtained over a region of about $5'$ centered at the position $\alpha(\text{J2000}) = 3^{\text{h}}29^{\text{m}}24^{\text{s}}$ and $\delta(\text{J2000}) = 31^\circ 8'$. This region covers the F1–F4 and F1p–F4p observed fields with the WHT (see Section 2.1). The CO spectra were retrieved from the COMPLETE data archive (Ridge et al. 2006b; Pineda et al. 2008). The dotted vertical line shows the systemic velocity of the IRAS 4A core (Choi 2001).

different telescope and observational technique. Therefore, the near-IR polarimetric capabilities of LIRIS have proved to be scientifically trustworthy for the astronomical community, and assure this mode will be useful for gathering measurements of objects experiencing high interstellar extinction inaccessible to optical instruments.

2. The polarization map obtained for the surveyed area is dominated by a well-ordered component produced by dichroic interstellar absorption. However, there are objects, some of them cataloged as YSOs, that show a transversal component which may be generated by internal scattering within circumstellar disks.
3. The magnetic field morphology traced by the near-IR/optical map is almost perpendicular with respect to the field morphology obtained with the submillimeter data toward the dense molecular core around IRAS 4A/4B. The near-IR/optical polarimetric data trace the field morphology of the diffuse molecular gas, which is known to have a multi-velocity structure. That is, the observed resulting magnetic field direction is probably the averaged magnetic field over several distinct velocity components of the cloud. CO molecular data obtained for this line of sight show non-Gaussian line profiles that are consistent with this hypothesis.

F.O.A. acknowledges the hospitality of the Instituto de Astrofísica de Canarias, where part of this work was developed. The authors thank the staffs of the Observatorio del Roque de los Muchachos and Observatório do Pico dos Dias for their hospitality and invaluable help during the observing runs. We also appreciate Terry Mahoney’s help with the manuscript. We made extensive use of NASA’s Astrophysics Data System (NASA/ADS) and the SIMBAD database, operated at CDS, Strasbourg, France. CO spectra were retrieved from the COMPLETE Survey of Star-forming Regions (Goodman 2004; Ridge et al. 2006b). This publication makes use of data products from the Two

Micron All Sky Survey, which is a joint project of the University of Massachusetts and the Infrared Processing and Analysis Center/California Institute of Technology, funded by the National Aeronautics and Space Administration and the National Science Foundation. G.A.P.F. acknowledges a grant from Fundación Carolina (Spain). This research has been partially supported by AYA2008-06189-C03 and AYA2004-03136 (Ministerio de Ciencia e Innovación, Spain), CEX APQ-1130-5.01/07 (FAPEMIG, Brazil), CNPq (Ministério da Ciência e Tecnologia, Brazil), and 2009SGR1172 (AGAUR, Generalitat de Catalunya).

REFERENCES

- Acosta-Pulido, J. A., Barrena-Delgado, R., Ramos-Almeida, C., & Manchado-Torres, A. 2006, in *Scientific Detectors for Astronomy 2005*, ed. J. E. Beletic, J. W. Beletic, & P. Amico (Dordrecht: Springer), 521
- Acosta-Pulido, J. A., et al. 2003, *News. Isaac Newton Group Telesc.*, 7, 15
- Andersson, B.-G., & Potter, S. B. 2007, *ApJ*, 665, 369
- Angel, J. R. P. 1969, *ApJ*, 158, 219
- Anglada, G., Rodríguez, L. F., Osorio, M., Torrelles, J. M., Estalella, R., Beltrán, M. T., & Ho, P. T. P. 2004, *ApJ*, 605, L137
- Arce, H. G., Goodman, A. A., Bastien, P., Manset, N., & Sumner, M. 1998, *ApJ*, 499, L93
- Aspin, C. 2003, *AJ*, 125, 1480
- Aspin, C., Sandell, G., & Russell, A. P. G. 1994, *A&AS*, 106, 165
- Attard, M., Houde, M., Novak, G., Li, H., Vaillancourt, J. E., Dowell, C. D., Davidson, J., & Shinnaga, H. 2009, *ApJ*, 702, 1584
- Bastien, P., & Menard, F. 1990, *ApJ*, 364, 232
- Brown, J. C., & McLean, I. S. 1977, *A&A*, 57, 141
- Černis, K. 1990, *Ap&SS*, 166, 315
- Chen, X., Launhardt, R., & Henning, T. 2009, *ApJ*, 691, 1729
- Choi, M. 2001, *ApJ*, 553, 219
- Crutcher, R. M., Hakobian, N., & Troland, T. H. 2009, *ApJ*, 692, 844
- Davis, L. J., & Greenstein, J. L. 1951, *ApJ*, 114, 206
- Draine, B. T., & Weingartner, J. C. 1996, *ApJ*, 470, 551
- Franco, G. A. P., Alves, F. O., & Girart, J. M. 2010, *ApJ*, 723, 146
- Galli, D., & Shu, F. H. 1993, *ApJ*, 417, 243
- Gerakines, P. A., Whittet, D. C. B., & Lazarian, A. 1995, *ApJ*, 455, L171
- Getman, K. V., Feigelson, E. D., Townsley, L., Bally, J., Lada, C. J., & Reipurth, B. 2002, *ApJ*, 575, 354
- Girart, J. M., Crutcher, R. M., & Rao, R. 1999, *ApJ*, 525, L109
- Girart, J. M., Rao, R., & Marrone, D. P. 2006, *Science*, 313, 812
- Gonçalves, J., Galli, D., & Girart, J. M. 2008, *A&A*, 490, L39
- Goodman, A. A. 2004, in *ASP Conf. Ser. 323, Star Formation in the Interstellar Medium: In Honor of David Hollenbach*, ed. D. Johnstone, F. C. Adams, D. N. C. Lin, D. A. Neufeld, & E. C. Ostriker (San Francisco, CA: ASP), 171
- Goodman, A. A., Bastien, P., Menard, F., & Myers, P. C. 1990, *ApJ*, 359, 363
- Goodman, A. A., Jones, T. J., Lada, E. A., & Myers, P. C. 1992, *ApJ*, 399, 108
- Goodman, A. A., Jones, T. J., Lada, E. A., & Myers, P. C. 1995, *ApJ*, 448, 748
- Herbig, G. H. 1974, *Lick Obs. Bull.*, 658, 1
- Hoang, T., & Lazarian, A. 2008, *MNRAS*, 388, 117
- Hoang, T., & Lazarian, A. 2009, *ApJ*, 697, 1316
- Itoh, Y., Gupta, R., Oasa, Y., Sen, A. K., Tanaka, M., Terai, T., & Nakaoka, S. 2010, *PASJ*, 62, 1149
- Knee, L. B. G., & Sandell, G. 2000, *A&A*, 361, 671
- Lada, C. J., Alves, J., & Lada, E. A. 1996, *AJ*, 111, 1964
- Lada, C. J., Gottlieb, C. A., Litvak, M. M., & Lilley, A. E. 1974, *ApJ*, 194, 609
- Lazarian, A. 2007, *J. Quant. Spectrosc. Radiat. Transfer*, 106, 225
- Lazarian, A., & Hoang, T. 2007, *MNRAS*, 378, 910
- Magalhães, A. M., Rodrigues, C. V., Margoniner, V. E., Pereyra, A., & Heathcote, S. 1996, in *ASP Conf. Ser. 97, Polarimetry of the Interstellar Medium*, ed. W. G. Roberge & D. C. B. Whittet (San Francisco, CA: ASP), 118
- Manchado, A., et al. 2004, *Proc. SPIE*, 5492, 1094
- McMillan, R. S. 1978, *ApJ*, 225, 880
- Menard, F., & Bastien, P. 1992, *AJ*, 103, 564
- Mouschovias, T. 2001, in *ASP Conf. Ser. 248, Magnetic Fields Across the Hertzsprung–Russell Diagram*, ed. G. Mathys, S. K. Solanki, & D. T. Wickramasinghe (San Francisco, CA: ASP), 515
- Mouschovias, T. C., & Tassis, K. 2010, *MNRAS*, 409, 801
- Mundt, R., & Fried, J. W. 1983, *ApJ*, 274, L83
- Naghizadeh-Khouei, J., & Clarke, D. 1993, *A&A*, 274, 968
- Oliva, E. 1997, *A&AS*, 123, 589
- Olmi, L., Testi, L., & Sargent, A. I. 2005, *A&A*, 431, 253
- Pereyra, A., Girart, J. M., Magalhães, A. M., Rodrigues, C. V., & de Araújo, F. X. 2009, *A&A*, 501, 595
- Pineda, J. E., Caselli, P., & Goodman, A. A. 2008, *ApJ*, 679, 481
- Quillen, A. C., Thorndike, S. L., Cunningham, A., Frank, A., Gutermuth, R. A., Blackman, E. G., Pipher, J. L., & Ridge, N. 2005, *ApJ*, 632, 941
- Ridge, N. A., Schnee, S. L., Goodman, A. A., & Foster, J. B. 2006a, *ApJ*, 643, 932
- Ridge, N. A., et al. 2006b, *AJ*, 131, 2921
- Rodríguez, L. F., Anglada, G., Torrelles, J. M., Mendoza-Torres, J. E., Haschick, A. D., & Ho, P. T. P. 2002, *A&A*, 389, 572
- Sandell, G., & Knee, L. B. G. 2001, *ApJ*, 546, L49
- Schmidt, G. D., Elston, R., & Lupie, O. L. 1992, *AJ*, 104, 1563
- Serkowski, K. 1974, in *Methods of Experimental Physics*, Vol. 12A, ed. N. Carleton (New York: Academic), 361
- Serkowski, K., Mathewson, D. S., & Ford, V. L. 1975, *ApJ*, 196, 261
- Shu, F. H., Adams, F. C., & Lizano, S. 1987, *ARA&A*, 25, 23
- Shu, F. H., Galli, D., Lizano, S., & Cai, M. 2006, *ApJ*, 647, 382
- Simmons, J. F. L., & Stewart, B. G. 1985, *A&A*, 142, 100
- Strom, S. E., Grasdalen, G. L., & Strom, K. M. 1974, *ApJ*, 191, 111
- Tamura, M., Yamashita, T., Sato, S., Nagata, T., & Gatley, I. 1988, *MNRAS*, 231, 445
- Turnshek, D. A., Turnshek, D. E., & Craine, E. R. 1980, *AJ*, 85, 1638
- Ungerechts, H., & Thaddeus, P. 1987, *ApJS*, 63, 645
- Vaillancourt, J. E., et al. 2008, *ApJ*, 679, L25
- Vrba, F. J., Strom, S. E., & Strom, K. M. 1976, *AJ*, 81, 958
- Walsh, A. J., Myers, P. C., Di Francesco, J., Mohanty, S., Bourke, T. L., Gutermuth, R., & Wilner, D. 2007, *ApJ*, 655, 958
- Wardle, J. F. C., & Kronberg, P. P. 1974, *ApJ*, 194, 249
- Warin, S., Castets, A., Langer, W. D., Wilson, R. W., & Pagani, L. 1996, *A&A*, 306, 935
- Whittet, D. C. B., Hough, J. H., Lazarian, A., & Hoang, T. 2008, *ApJ*, 674, 304
- Whittet, D. C. B., Martin, P. G., Hough, J. H., Rouse, M. F., Bailey, J. A., & Axon, D. J. 1992, *ApJ*, 386, 562
- Wilking, B. A., Meyer, M. R., Greene, T. P., Mikhail, A., & Carlson, G. 2004, *AJ*, 127, 1131